ACS Photonics

pubs.acs.org/journal/apchd5 Article

Engineering Nanoparticles with Pure High-Order Multipole Scattering

Vladimir A. Zenin,*,△ Cesar E. Garcia-Ortiz,△ Andrey B. Evlyukhin,* Yuanqing Yang, Radu Malureanu, Sergey M. Novikov, Victor Coello, Boris N. Chichkov, Sergey I. Bozhevolnyi, Andrei V. Lavrinenko, and N. Asger Mortensen

Cite This: *ACS Photonics* 2020, 7, 1067−1075 Read Online

ACCESS | Metrics & More | Article Recommendations | Supporting Information

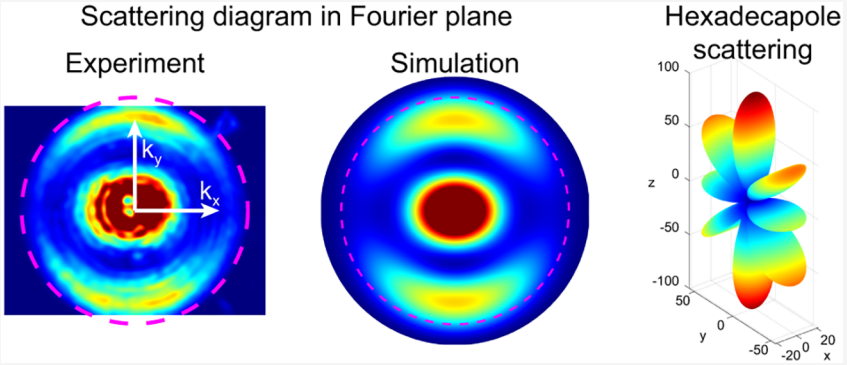

ABSTRACT: The ability to control scattering directionality of nanoparticles is in high demand for many nanophotonic applications. One of the challenges is to design nanoparticles producing pure high-order multipole scattering (e.g., octopole, hexadecapole), whose contribution is usually negligible compared with strong low-order multipole scattering (i.e., dipole or quadrupole). Here we present an intuitive way to design such nanoparticles by introducing a void inside them. We show that both shell and ring nanostructures allow regimes with nearly pure high-order multipole scattering. Experimentally measured scattering diagrams from properly designed silicon rings at near-infrared wavelengths (~800 nm) reproduce well scattering patterns of an electric octopole and magnetic hexadecapole. Our findings advance significantly inverse engineering of nanoparticles from given complex scattering characteristics, with possible applications in biosensing, optical metasurfaces, and quantum communications.

KEYWORDS: *multipole decomposition, all-dielectric nanoparticles, scattering diagram, octopole, hexadecapole*

Modern photonic applications involve manipulation of light at the nanoscale by means of optical resonances. There are two main families of such resonances: polaritonic resonances originating from strongly dispersive negative dielectric permittivities (for example, plasmon-polariton resonances, supported by metallic nanoparticles) and photonic resonances utilizing high-refractive-index dielectric materials.[1,2] The latter is highly beneficial because of low, almost negligible absorption losses, compatibility with well-established semiconductor fabrication processes, and abundance of different optical modes (and corresponding resonances) even for simple symmetric shapes of dielectric nanoparticles.[3−5] The above advantages led to a broad variety of applications utilizing dielectric nanoparticles, including light manipulation with metasurfaces,[6−11] color printing,[12,13] lasing,[14,15] biosensing,[16−18] strong coupling,[19−22] and applications within quantum optics and topological photonics.[23−25]

The optical properties of nanoparticles can be analyzed in different ways. One of the analytical tools is the multipolar decomposition, in which a generally complex field scattered by a nanoantenna is replaced by the superposition of fields (with relatively simple patterns) generated by basic point sources, called multipole moments, corresponding to the nanoantenna's current distributions.[26] The number and type of multipole moments, which are sufficient to faithfully describe the scattered fields, are determined by the size, shape, and composition of nanoantennas. There are two basic approaches to the multipole decomposition of the scattered fields. The first is obtained from the Taylor expansion for the retarded potentials of electromagnetic fields generated by the induced electric currents in the nanoantennas. In this case, the

Received: January 16, 2020
Published: February 28, 2020

https://dx.doi.org/10.1021/acsphotonics.0c00078
ACS Photonics 2020, 7, 1067−1075

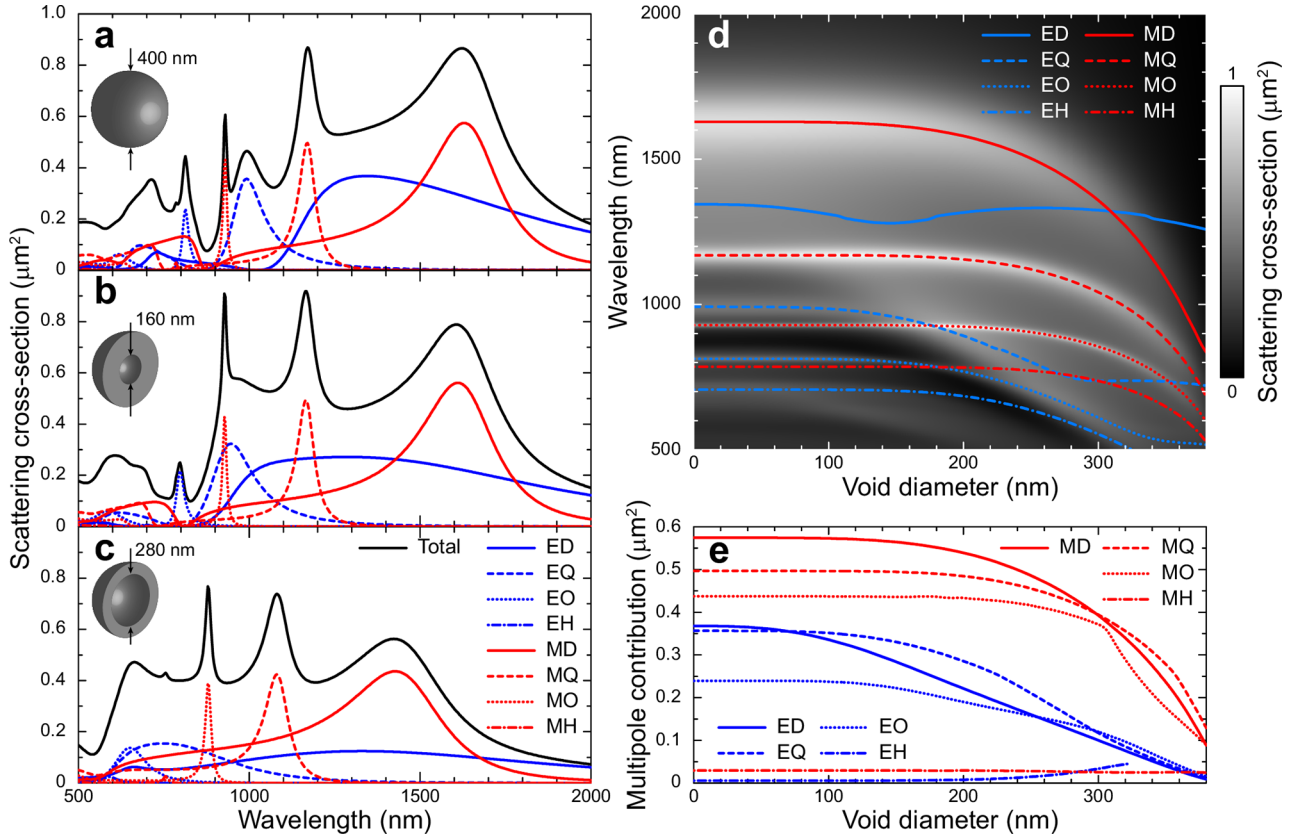

Figure 1. Evolution of scattering upon nanoparticle transformation from a solid sphere into a shell. (a–c) Total scattering cross-section (black) and individual contributions from electric (blue) and magnetic multipoles (red) for a silicon sphere without a void (a) and with a void diameter of 160 nm (b) and 280 nm (c). Here ED, EQ, EO, and EH stand for electrical dipole, quadrupole, octopole and hexadecapole, respectively, while MD, MQ, MO, MH stand for the corresponding magnetic multipoles. The outer diameter of Si sphere/shell is 400 nm. The refractive index of the surroundings and inside the void is assumed to be $n = 1.48$. (d) Total SCS as a function of the free-space wavelength and void diameter for the Si sphere/shell particle. Resonances for electric (blue) and magnetic multipoles (red) are shown with lines. (e) Contributions of electric (blue) and magnetic multipoles (red) to the total SCS along their resonance curves as a function of the void diameter.

multipole moments are determined as coefficients of the expansion and include ordinary multipole moments[27] and the so-called mean-square radii[28−31] or high-order toroidal moments.[32,33] The far-field nanoantenna scattering is, on the other hand, rational to describe in terms of angular distributions in the spherical coordinate system with the nanoantenna being in its center. Therefore, the second approach is based on the decomposition of a scattered far field into a series of the spherical harmonics, which form a natural basis in the spherical coordinate system and are assigned to the corresponding spherical multipoles.[26] In this case, the multipole moments are directly calculated from the distribution of scattered electric field on any spherical surface enclosing the nanoantenna.[34] By expressing the generated field on the spherical surface through the source currents, the spherical multipole moments can also be calculated using the current distributions induced inside the nanoantenna.[26,34−36] Recently, another point of view showed the similarity and differences between the above-mentioned two approaches to the multipole decomposition.[37] In this work, we focus only on the far-field scattering; therefore, only the spherical multipole decomposition is applied.

Similarly to Taylor series, where the first couple of terms represents usually the largest contribution in the expansion, only low-order multipole terms (dipoles, quadrupoles) contribute most to the total scattering from small nanoantennas, while contributions from high-order multipole terms (octopoles, hexadecapoles, and so on) are generally negligible. It is thus a nontrivial problem to find a nanoparticle, whose scattering is dominated by a contribution from high-order multipole moments. One way to get a considerable high-order multipole response is to increase the scatterer size. However, even for large scatterers, the high-order multipole contribution appears to be weak compared to strong contributions from the low-order multipole moments. Only when the multipole resonances are narrow enough and spectrally well separated, one might get a pure high-order multipole scattering in a narrow wavelength range (which, we believe, is the case for whispering gallery resonators). Here, we provide a direct method for designing high-order multipole scatterers by introducing a void inside a nanoparticle without modifying its external dimensions. First, using numerical simulations, we consider the evolution of multipole moments when increasing the diameter of a concentric spherical void inside a dielectric sphere, transforming eventually the latter into a shell nanoparticle. We find that, by introducing the void, the total scattering strength as well as the contribution from each multipole moment decreases. However, the reduction is stronger for the low-order multipole terms so that the relative contribution from the high-order multipole moments grows with the increase of the void. The same trend is also found for disk nanostructures, and we show that certain Si ring

https://dx.doi.org/10.1021/acsphotonics.0c00078
ACS Photonics 2020, 7, 1067−1075

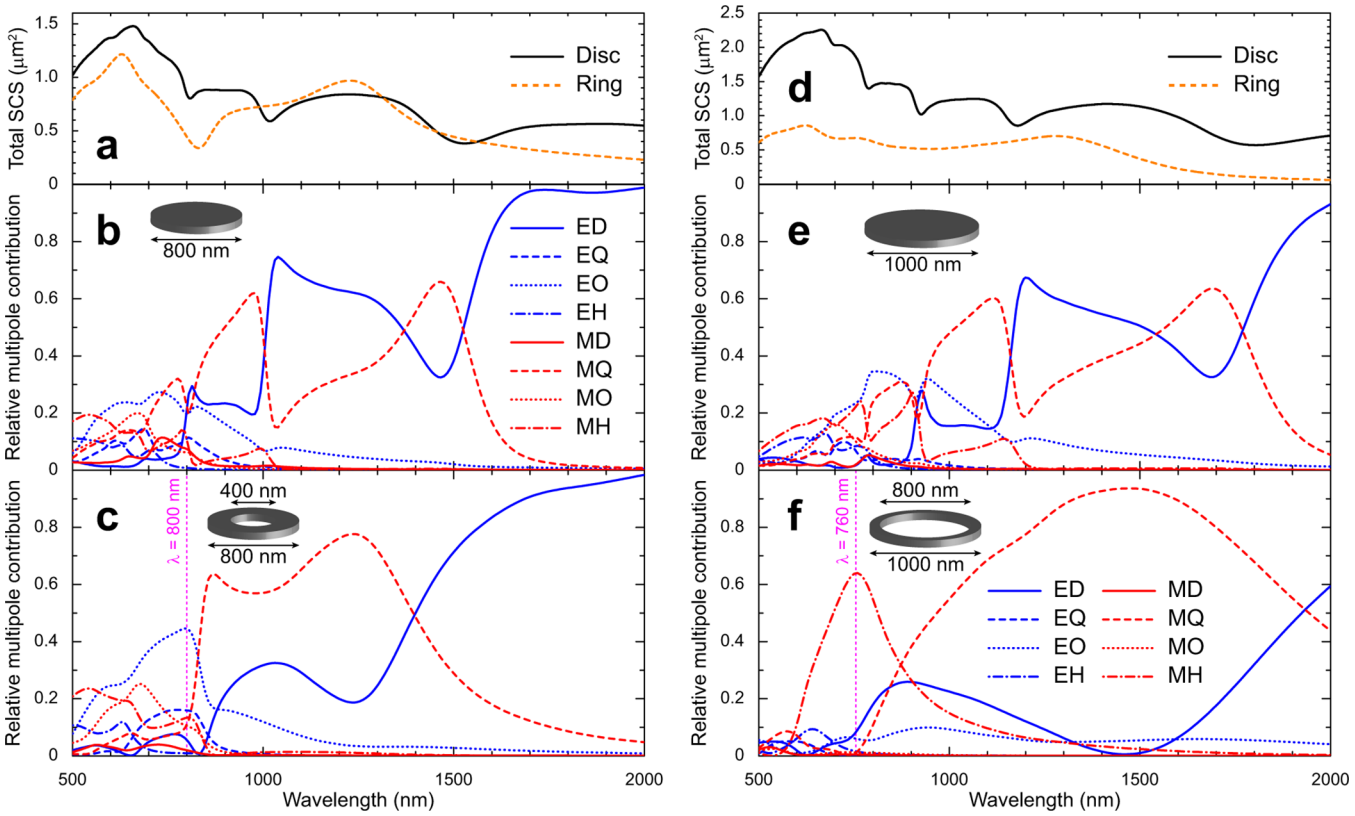

Figure 2. Multipole analysis of disk and ring scattering. (a,d) Total SCS of the disk (solid black) and ring (dashed orange) with (a) 400/800 nm and (d) 800/1000 nm inner/outer diameter, respectively. (b,c) Relative contributions from electric (blue) and magnetic multipoles (red) to the total SCS for the disk (b) and ring (c) with the inner/outer diameter of 400/800 nm. (e,f) Relative contributions from electric (blue) and magnetic multipoles (red) to the total SCS for the disk (e) and ring (f) with the inner/outer diameter of 800/1000 nm. The ring thickness is 80 nm, and the refractive index of surrounding is assumed to be $n = 1.48$. Magenta line indicates the wavelength, at which the scattering is dominated by electric octopole (c) or magnetic hexadecapole (f) contribution.

nanostructures scatter practically as the pure electric octopole or magnetic hexadecapole at the wavelength of 800 nm. This is verified by direct experimental measurements of the scattering diagram from individual nanoparticles. Our findings can be applied in biosensing, where narrow-band resonances and complex scattering patterns can boost the sensitivity and resolution. In a more general sense, our results significantly advance inverse engineering of nanoparticles, where the nanoparticle shape is to be obtained from given scattering properties. Finally, nanoparticles with such peculiar scattering properties can advantageously be used as meta-atoms for the design of metasurfaces exhibiting required complex functionalities. Particularly, it was recently shown that the high-order multipole term of scatterers is required in order to achieve full 2π phase coverage of Huygens' metasurface elements.[38]

SCATTERING OF SPHERE AND SHELL NANOPARTICLES

We begin by numerically analyzing the scattering produced by a Si nanoparticle of the simplest morphology—a sphere, where we introduce a void in the center and gradually transform the solid sphere into a shell (Figure 1). Throughout the rest of the work, the refractive index of Si is taken from measurements of a deposited amorphous Si (see Supporting Information, Figure S1), and the outer diameter of the sphere and shell particles is fixed to 400 nm. Mie theory[39,40] was used to calculate the total scattering cross-section (SCS) and multipole decomposition (see Supporting Information, Figures S2−S3). We found that the contribution from each multipole (except for the electric dipole) to the total SCS has a resonance-shape dependence on the wavelength, that is, there is a well-defined peak (see Supporting Information, Figure S2), whose position was determined for every void diameter and plotted on top of the total SCS map (Figure 1d). These resonances are narrow and well-separated, so one can get nearly pure high-order multipole scattering (electric and magnetic quadrupole, and magnetic octopole) for a solid Si sphere (Figure 1a). A nearly pure electric octopole (EO) scattering can be found for the Si shell particle with the void diameter of 160 nm (Figure 1b, at $\lambda \approx 800$ nm). Finally, by increasing the void diameter further to 280 nm, one can enable a magnetic octopole (MO) resonance well-separated from all other multipole resonances, thus having its dominant contribution in a broad wavelength range (Figure 1c, at $\lambda \approx 870$ nm). The dominant multipole and its relative contribution to the total SCS for varied void diameter can be found in Supporting Information, Figure S3.

In order to analyze the influence of the void size on the response of each multipole, we calculated their contribution to the total SCS at the resonance wavelength of the multipole (Figure 1e). By increasing the void size, the total SCS and contributions from each multipole at its resonance decrease with a blueshift of their peaks (Figure 1d,e). This is expected because the total volume of Si is reduced. However, the scattering contributions from the low-order multipoles decrease faster compared with the high-order multipoles. Additionally, the contributions from electric multipoles

https://dx.doi.org/10.1021/acsphotonics.0c00078
ACS Photonics 2020, 7, 1067−1075

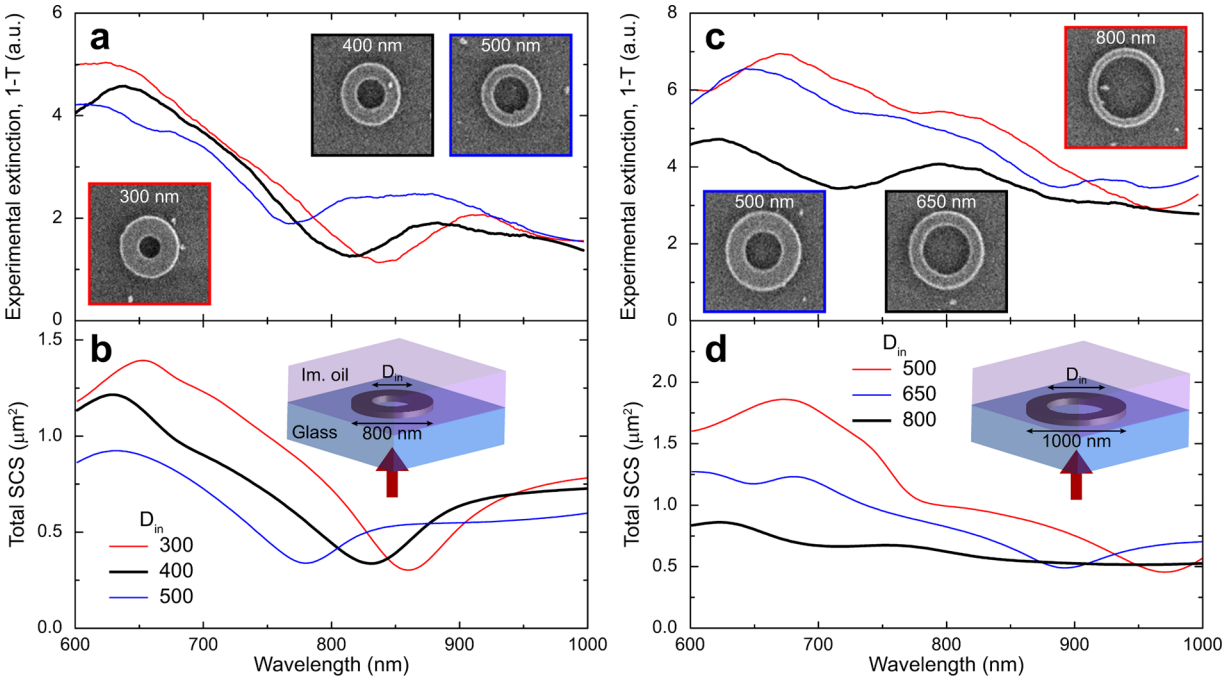

Figure 3. (a,c) Experimental far-field extinction spectra ($1 - T$) and (b,d) simulated scattering spectra of Si rings with varied internal hole diameter D_{in} and external diameter of 800 nm (a,b) and 1000 nm (c,d), respectively. In experiments, the substrate is glass ($n \approx 1.45$), and the superstrate is immersion oil ($n = 1.518$). The rings are illuminated from the glass side (illustrated with red arrow). In simulations, the ring is embedded evenly in the surrounding environment with the refractive index of $n = 1.48$. Insets show SEM images of the structures, with labeled inner void diameter (panel size: 1500 nm).

decrease faster compared with magnetic multipoles. This can be explained as following: the multipole moment is proportional to the volume integral of $j^m(kr)\Pi(\mathbf{r}^m, \mathbf{j})/r^m$, where j_m is the m-th order spherical Bessel function of the first kind, $k = 2\pi n/\lambda$ is the wavenumber in the surrounding environment, $\mathbf{j}$ is the induced electric current density, $\mathbf{r}$ is the radius vector of the observation point, $\Pi(\mathbf{r}^m, \mathbf{j})$ is the combination of vector and scalar product between $\mathbf{j}$ and m-times $\mathbf{r}$, and the integration is done over the volume of the particle.[35,37] In the above expression, $m = n$ for magnetic multipoles of order n, where $n = 1$ means dipole, $n = 2$—quadrupole, and so on. Electric multipole moments of order n consist of two terms, each having the above expression, but with $m = n - 1$ for the first term (which is usually dominating), and with $m = n + 1$ for the second term (which is usually a small correction, relative to the first term). Thus, the spherical Bessel function acts as a weight inside the integration; therefore, the lower the multipole order, the smaller it is influenced by the suppression of the central part. The zero-order spherical Bessel function is the only one having nonzero value at the origin (see Supporting Information, Figure S2i); therefore, it is only the electric dipole contribution which is significantly influenced by the introduction of a small void (Figure 1e). The interplay between the order-dependent suppression of the multipole contribution and shifts of the resonances results in the complex variation of the high-order multipole purity (see Supporting Information, Figure S3).

SCATTERING OF DISK AND RING NANOPARTICLES

In order to test the generality of our findings, we replaced a sphere with its flat analog—a disk—and transformed it into a ring by introducing a void in its center (Figure 2). It appeared that for the disk/ring structure, multipole spectra do not have simple resonance shapes as for the sphere/shell particle, and an evolution of these spectra with a change of the void size is rather complicated (see Supporting Information, Figures S4–S7). However, the general trend remains the same: with the increase of the hole the contributions from low-order multipoles decrease faster compared with the high-order multipoles. Additionally, because of the symmetry and small thickness of the particle, the contributions from electric multipoles of the odd order and magnetic multipoles of the even order are negligible, simplifying the quest to find a regime with nearly pure high-order multipole scattering. We found that at the wavelength around $\lambda \approx 800$ nm and ring thickness of 80 nm, the scattering is dominated by the electric octopole (EO) for the ring with the inner/outer diameter of 400/800 nm (Figure 2c), and it is dominated by the magnetic hexadecapole (MH) for the ring with the inner/outer diameter of 800/1000 nm (Figure 2f). Here, the total scattering is calculated by numerical simulations (see Methods), from which multipole contributions are calculated, using the electric field inside the particle (in a same way as in our previous works[41,42]). The peak purity of high-order multipole scattering, that is, their relative contributions to the total SCS, was found to be ~45% for EO (Figure 2c) and ~65% for MH (Figure 2f).

Even though the particle size is comparable to the operating wavelength, it does not prohibit the use of such particles as building blocks of metasurfaces. The main design target is that the metasurface configuration funnels most of the incident radiation into only one diffraction order. This can be achieved either by assembling small different meta-atoms into periodic supercells or by using large identical meta-atoms with complex responses.[7] Despite the high-order multipole response being not resonant, one could still employ these particles in sensing

https://dx.doi.org/10.1021/acsphotonics.0c00078
ACS Photonics 2020, 7, 1067–1075

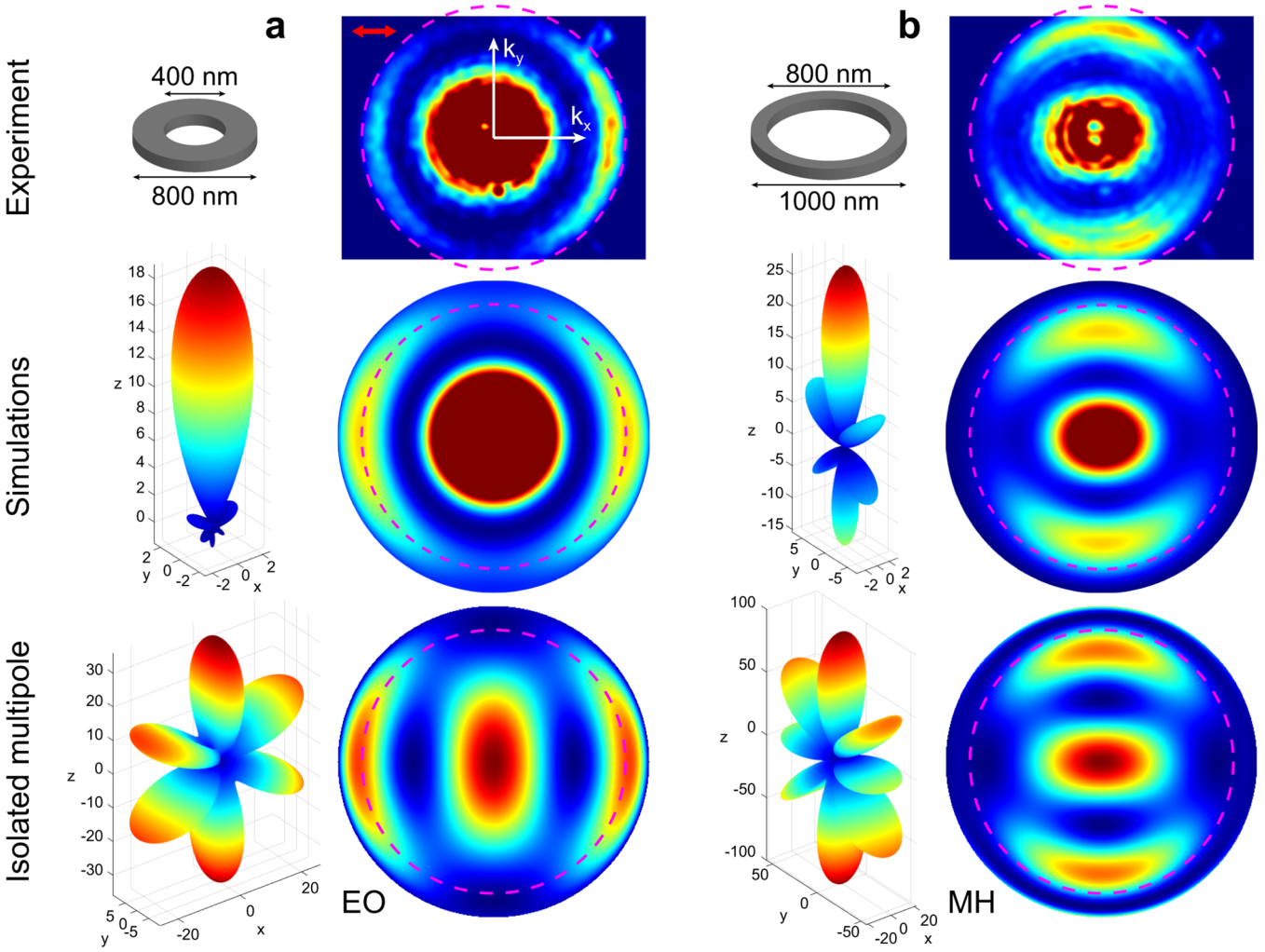

Figure 4. Scattering diagrams of Si rings. (a,b) Experimentally measured and simulated scattering diagrams of Si rings with (a) 400/800 nm and (b) 800/1000 nm inner/outer diameter, respectively, compared with radiation diagrams of isolated (a) electric octopole (EO) and (b) magnetic hexadecapole (MH). The incident polarization is illustrated with a red arrow in (a). Magenta line in Fourier plane images shows the experimental limit for the collection angle and corresponds to the NA of the immersion-oil objective (1.25).

by arranging them into a periodic array that would support lattice resonances with sharp features in transmission or reflection spectra.

To confirm such selective scattering, we fabricated a series of isolated 80 nm-thick Si rings with a varied inner (void) diameter and a fixed outer diameter of 800 and 1000 nm, respectively. The fabrication was done by deposition of amorphous Si on a glass substrate, followed by etching through the mask (see Methods). First we measured the far-field transmission T for each ring (see Methods), plot it as extinction $1 - T$, and compared with simulated total scattering (Figure 3).

One can already note from Figure 2 that the region with the dominant scattering by a single high-order multipole is not reflected in the total scattering spectrum. However, there are still some distinct features in spectra (dips and peaks); therefore, by comparing them in measurements and simulations (Figure 3), one can indirectly verify the correspondence between simulations and experiments.

Then we proceeded to direct measurements of the scattering diagram of Si rings (see Methods). The experimentally measured scattering diagrams of rings with 400/800 nm and 800/1000 nm inner/outer diameter are shown in Figure 4, compared with simulated total scattering diagram and analytically calculated radiation pattern of an isolated multipole. Regarding the latter, one can directly calculate contributions of the selected multipoles to the scattering diagram,[37] when their multipole moment is known (traceless and symmetrical tensors of rank 3 for octopole and rank 4 for hexadecapole). However, to simplify the analysis, we used direct expressions for the scattering diagrams of these multipoles for a perfect sphere in an even dielectric environment:[40,43]

$$\sigma_{EO}(\theta, \varphi) \propto \cos^2 \varphi[(5\cos^2\theta - 1)]^2 + \sin^2 \varphi[\cos\theta(15\cos^2\theta - 11)]^2,$$

$$\sigma_{MH}(\theta, \varphi) \propto \sin^2 \varphi[\cos\theta(7\cos^2\theta - 3)]^2 + \cos^2 \varphi[(28\cos^4\theta - 27\cos^2\theta + 3)]^2,$$

where θ and φ are the polar and azimuthal angles, respectively, and E (M) stands for electric (magnetic) multipole (see Supporting Information, Supplementary Note 1). Though dependence of multipole contributions on the wavelength and void size for the disk/ring structure is quite different than that of the sphere/shell particle, we expect similar scattering

https://dx.doi.org/10.1021/acsphotonics.0c00078
ACS Photonics 2020, 7, 1067−1075

diagrams for isolated multipoles of these particles due to the same mirror symmetry of the sphere and the ring. The above assumption and the validity of simulations in general are verified by a good agreement between experiment, simulations, and analytical calculations (Figure 4).

Moreover, the scattering diagrams have a well-pronounced feature—scattering side-lobes along (Figure 4a) or across the orientation of the incident beam polarization (Figure 4b), which is a clear indication of the electric or magnetic multipole scattering. In case of the small ring with the inner/outer diameter of 400/800 nm (Figure 4a), scattering side-lobes are at around NA ≈ 1.25 in the Fourier plane, corresponding to the angle of $\arcsin(1.25/1.48) \approx \pi/3$, clearly confirming its electric octopole origin (see Supplementary Note 1). As for the other ring with the inner/outer diameter of 800/1000 nm (Figure 4b), scattering side-lobes reach the maximum at around NA ≈ 1 in the Fourier plane, corresponding to the angle of $\arcsin(1/1.48) \approx \pi/4$, which is in accordance with the magnetic hexadecapole. Interestingly, the number of principal scattering lobes (6 for octopole and 8 for hexadecapole) cannot be anticipated from the multipole name, but it rather follows $2n$, where n is the multipole order. This is not a contradiction, because the multipole name reflects the minimum number of oscillating point charges required to produce the given multipole moment, while it doesn't state the number of scattering lobes. The deviation between scattering diagrams of each ring and the radiation pattern of the corresponding isolated multipole is due to the interference with other multipoles' contributions (16% from EQ, 13% from MH, 11% from MO, and 10% from MQ for the small ring; and 19% from ED, 12% from MQ, and 6% from EO for the large ring, as follows from Figure 2 at λ = 800 nm). This interference can lead to a strong suppression of some scattering lobes, but their angular positions are only slightly affected, which is an indication of the dominating single high-order multipole contribution (see Supporting Information, Figure S9, for more discussion). The resulted asymmetry in forward/backward scattering is the so-called Mie effect,[39,44] which is a transition between symmetric Rayleigh scattering and diffraction.

Finally, we compiled animations showing the evolution of simulated scattering for the above structures by gradually decreasing the wavelength (see Supplementary Movies S1 and S2), where one can verify that the strongly pronounced and polarization-dependent scattering lobes are indeed a feature of the nearly pure high-order multipole scattering.

CONCLUSIONS

In summary, we demonstrated that the relative contribution of high-order multipoles can be boosted by introducing the void inside a high-refractive index nanoparticle. Using such a method allows finding a composition of the nanoparticle, whose scattering will be dominated by a single high-order multipole. We proved this method on a disk/ring shape, using Si as a high-refractive index material with a thickness of 80 nm. First, we numerically found two structures producing nearly pure electric octopole and magnetic hexadecapole scattering. Then we fabricated such structures, directly measured their scattering diagrams, and finally verified the dominant high-order multipole contribution. In addition to providing an intuitive understanding of the relation between shape and multipoles, our results can directly benefit applications in metasurfaces, sensing, quantum communications, and topological photonics.

METHODS

Fabrication. The rings were fabricated by etching amorphous silicon, deposited on a silica wafer. First, the fresh silica wafer was cleaned using a standard RCA clean, without the HF steps. Then 80 nm of Si was deposited using low-pressure chemical vapor deposition (LPCVD). Depending on the growth temperature, the LPCVD can grow crystalline or amorphous Si. In our case, we grew Si at 560 °C, a standard recipe for our lab that grows amorphous Si. The polycrystalline Si is typically grown at 620 °C. Other process parameters are 80 sccm Silane flow, 200 mTorr pressure. The growth rate is typically 2.5 nm/min. The procedure implies growing on a test wafer to measure the actual growth rate and then calibrate the growth time. The obtained thickness is generally within 1% of the desired one. The Si thickness of 80 nm was chosen from practical considerations, because at this thickness, the lateral size of structures with dominating high-order EO and MH response at the operating wavelength of ∼800 nm is large enough for a precise control of the void size but not much larger than the operating wavelength. Standard reflectometry (FilmTek 4000TM) was used to measure Si thickness and refractive index (Supporting Information, Figure S1). After the Si deposition, AR-P 6200 resist from Allresist was spun at 200 nm, followed by thermal evaporation of 20 nm Al to be used as discharge path during the exposure. The structures were defined by electron-beam exposure. The next step involves Al layer removal in diluted phosphoric acid and development of the resist. The patterned resist is then used as a mask for etching the Si layer using a Bosch process and then removed using low power oxygen plasma.

Numerical Simulations. Scattering spectra, diagrams, and the electric field inside the structures (for multipole decomposition) were calculated using a 3D simulation with the finite-element method (FEM) implemented in a commercial software (COMSOL Multiphysics). A simulation sphere with a diameter of 2.4 μm was used with the perfectly matched layer at the outer boundary and a tetrahedral mesh with a wavelength-dependent mesh size of $\sim \lambda/24$ inside the silicon and $\sim \lambda/9$ for the rest. The convergence of the numerical results was verified with finer mesh. The silicon ring was excited by a normal-incident CW plane wave, whose wavelength was swept to calculate spectra. For all calculations, the permittivity value of Si was taken from measurements (Supporting Information, Figure S1), the refractive index of surrounding environment was set to 1.48. Additional simulations for the Si disk/ring structures with the asymmetric environment (n = 1.518 for the cladding and n = 1.45 for the substrate) showed no noticeable difference in the total scattering cross sections and scattering diagrams compared with the simulation results for the even surrounding with n = 1.48. We expect that the asymmetry in the surrounding will have a noticeable effect only when the refractive index contrast between the substrate and the cladding will be of the same order of magnitude as the contrast with the nanoparticle (whose refractive index is ∼4).

Measurements of the Scattering Diagram. Schematic diagram of the experimental setup for measuring scattering diagrams is shown in Supporting Information, Figure S8. The sample was illuminated using a linearly polarized Ti:sapphire laser, tuned at a wavelength of ∼800 nm. The laser beam was

https://dx.doi.org/10.1021/acsphotonics.0c00078
ACS Photonics 2020, 7, 1067−1075

weakly focused onto the sample using a 10× objective of numerical aperture NA = 0.20. The full-width-at-half-maximum of the focused beam spot was ∼5 μm. The scattered light was collected using a 63× oil-immersion collection objective, with a NA = 1.25. The structures on the sample were positioned facing the oil-immersion objective, embedded in the index-matching oil (n = 1.518). An imaging system, which consists of two lenses and two spatial filters, was used to image the back focal plane (BFP) of the collection objective with a charge-coupled device (CCD) camera. The BFP and its image are also referred to here as the Fourier plane, because it shows angular distribution of the scattering (i.e., scattering diagram). The two spatial filters have the following important functionalities. The first filter is a micrometric metallic ball (diameter ∼300 μm), glued on a glass substrate, and it is used to stop the directly transmitted light from reaching the CCD camera to avoid saturation. It is a Fourier-plane filter, and ideally it should be placed at the BFP inside the collection objective. Nevertheless, since the objective collimates the scattered light, the filter can be placed at the rear aperture of the objective and still produce the same filtering effect. The second filter is a pinhole, positioned at the image plane (focal point of the first lens), and is used to stop all the unwanted scattering from the surroundings of the nanostructure (i.e., from impurities in the glass substrate and oil). The images are captured with the CCD camera, located at the focal distance of the second lens, which matches with the Fourier plane.

Far-Field Spectroscopy. Transmission spectroscopy was performed on a standard inverted optical microscope (Zeiss Axio Observer), equipped with a halogen light source, modified detection path, and fiber-coupled spectrometer (Ocean Optics QE Pro). The light was collected using a 100× immersion-oil objective (Zeiss α Plan-FLUAR, NA = 1.45) and the same index-matching oil (n = 1.518). Schematically, the setup is similar to the one for measuring scattering diagrams (Supporting Information, Figure S8), allowing filtering both in Fourier and direct image planes. We used an iris diaphragm for Fourier plane to limit detected NA to ∼0.3 (in order to replicate measurements of transmitted plane wave), and another iris diaphragm was set as a filter in the image plane, corresponding to the area with a diameter of ∼3 μm in a sample plane (that is, when image plane was recorded by a camera, the opening was ∼3 times larger than the ring with the outer diameter of 1 μm). The measured transmission spectra were normalized on the transmission spectrum through the glass substrate without any structure.

■ ASSOCIATED CONTENT

Supporting Information

The Supporting Information is available free of charge at https://pubs.acs.org/doi/10.1021/acsphotonics.0c00078.

Refractive index of Si; multipole decomposition of Si sphere/shell and disk/ring structures; layout of the experimental setup for measuring scattering diagrams; analytical expressions for multipole scattering diagrams (Supplementary Note 1) (PDF)

Supplementary Movie S1: evolution of the scattering for the Si ring with 400/800 nm inner/outer diameter by gradually decreasing the wavelength (MP4)

Supplementary Movie S2: evolution of the scattering for the Si ring with 800/1000 nm inner/outer diameter by gradually decreasing the wavelength (MP4)

■ AUTHOR INFORMATION

Corresponding Authors

Vladimir A. Zenin − *Center for Nano Optics, University of Southern Denmark, 5230 Odense, Denmark;* orcid.org/0000-0001-5512-8288; Email: zenin@mci.sdu.dk

Andrey B. Evlyukhin − *Institute of Quantum Optics, Leibniz University Hannover, 30167 Hannover, Germany; Center for Photonics and 2D Materials, Moscow Institute of Physics and Technology, 141700 Dolgoprudny, Russia;* orcid.org/0000-0002-1801-6778; Email: a.b.evlyukhin@daad-alumni.de

Authors

Cesar E. Garcia-Ortiz − *CICESE, Unidad Monterrey, PIIT Apodaca, Nuevo Leon 66629, Mexico;* orcid.org/0000-0002-7224-6718

Yuanqing Yang − *Center for Nano Optics, University of Southern Denmark, 5230 Odense, Denmark;* orcid.org/0000-0001-7139-1254

Radu Malureanu − *Department of Photonics Engineering and National Centre for Micro- and Nano-Fabrication, Technical University of Denmark, DK-2800 Kgs. Lyngby, Denmark;* orcid.org/0000-0002-6093-5030

Sergey M. Novikov − *Center for Nano Optics, University of Southern Denmark, 5230 Odense, Denmark; Center for Photonics and 2D Materials, Moscow Institute of Physics and Technology, 141700 Dolgoprudny, Russia;* orcid.org/0000-0001-9943-3946

Victor Coello − *CICESE, Unidad Monterrey, PIIT Apodaca, Nuevo Leon 66629, Mexico*

Boris N. Chichkov − *Institute of Quantum Optics, Leibniz University Hannover, 30167 Hannover, Germany; Lebedev Physical Institute, 119333 Moscow, Russia*

Sergey I. Bozhevolnyi − *Center for Nano Optics and Danish Institute for Advanced Study, University of Southern Denmark, 5230 Odense, Denmark;* orcid.org/0000-0002-0393-4859

Andrei V. Lavrinenko − *Department of Photonics Engineering, Technical University of Denmark, DK-2800 Kgs. Lyngby, Denmark;* orcid.org/0000-0001-8853-2033

N. Asger Mortensen − *Center for Nano Optics and Danish Institute for Advanced Study, University of Southern Denmark, 5230 Odense, Denmark;* orcid.org/0000-0001-7936-6264

Complete contact information is available at: https://pubs.acs.org/10.1021/acsphotonics.0c00078

Author Contributions

△V.A.Z. and C.E.G.-O. contributed equally to this work.

Notes

The authors declare no competing financial interest.

■ ACKNOWLEDGMENTS

The authors acknowledge financial support from the European Research Council (the PLAQNAP project, Grant No. 341054) and the University of Southern Denmark (SDU2020 funding), from scholarship 299967. N.A.M. is a VILLUM Investigator supported by Villum Fonden (Grant No. 16498). C.E.G.-O and V.C. acknowledge the technical assistance of Fabiola Armenta with the experimental setup. V.C. and C.E.G.-O. acknowledge funding from CONACYT Basic Scientific Research Grants No. 250719 and No. 252621. RM and AVL acknowledge the financial support from Villum Fonden "DarkSILD project" (Grant No. 11116) as well as the support of the National Centre for Nano Fabrication and Character-

ization (DTU Nanolab) for fabrication of the structures. A.B.E. and B.N.C. acknowledge financial support from the Deutsche Forschungsgemeinschaft (DFG, German Research Foundation) under Germany's Excellence Strategy within the Cluster of Excellence PhoenixD (EXC 2122, Project No. 390833453), the Cluster of Excellence QuantumFrontiers (EXC 2123, Project No. 390837967), and DFG Project CH179/34-1. Numerical simulation was partially supported by the Russian Science Foundation (Grant No. 18-19-00684).

REFERENCES

(1) Evlyukhin, A. B.; Reinhardt, C.; Seidel, A.; Luk'yanchuk, B. S.; Chichkov, B. N. Optical response features of Si-nanoparticle arrays. *Phys. Rev. B: Condens. Matter Mater. Phys.* **2010**, *82*, 045404.

(2) Evlyukhin, A. B.; Novikov, S. M.; Zywietz, U.; Eriksen, R. L.; Reinhardt, C.; Bozhevolnyi, S. I.; Chichkov, B. N. Demonstration of Magnetic Dipole Resonances of Dielectric Nanospheres in the Visible Region. *Nano Lett.* **2012**, *12*, 3749−3755.

(3) Kuznetsov, A. I.; Miroshnichenko, A. E.; Brongersma, M. L.; Kivshar, Y. S.; Luk'yanchuk, B. Optically resonant dielectric nanostructures. *Science* **2016**, *354*, aag2472.

(4) Staude, I.; Schilling, J. Metamaterial-inspired silicon nanophotonics. *Nat. Photonics* **2017**, *11*, 274−284.

(5) Baranov, D. G.; Zuev, D. A.; Lepeshov, S. I.; Kotov, O. V.; Krasnok, A. E.; Evlyukhin, A. B.; Chichkov, B. N. All-dielectric nanophotonics: the quest for better materials and fabrication techniques. *Optica* **2017**, *4*, 814−825.

(6) Shibanuma, T.; Matsui, T.; Roschuk, T.; Wojcik, J.; Mascher, P.; Albella, P.; Maier, S. A. Experimental Demonstration of Tunable Directional Scattering of Visible Light from All-Dielectric Asymmetric Dimers. *ACS Photonics* **2017**, *4*, 489−494.

(7) Khaidarov, E.; Hao, H.; Paniagua-Domínguez, R.; Yu, Y. F.; Fu, Y. H.; Valuckas, V.; Yap, S. L. K.; Toh, Y. T.; Ng, J. S. K.; Kuznetsov, A. I. Asymmetric Nanoantennas for Ultrahigh Angle Broadband Visible Light Bending. *Nano Lett.* **2017**, *17*, 6267−6272.

(8) Paniagua-Domínguez, R.; Yu, Y. F.; Khaidarov, E.; Choi, S.; Leong, V.; Bakker, R. M.; Liang, X.; Fu, Y. H.; Valuckas, V.; Krivitsky, L. A.; Kuznetsov, A. I. A Metalens with a Near-Unity Numerical Aperture. *Nano Lett.* **2018**, *18*, 2124−2132.

(9) Bucher, T.; Vaskin, A.; Mupparapu, R.; Löchner, F. J. F.; George, A.; Chong, K. E.; Fasold, S.; Neumann, C.; Choi, D.-Y.; Eilenberger, F.; Setzpfandt, F.; Kivshar, Y. S.; Pertsch, T.; Turchanin, A.; Staude, I. Tailoring Photoluminescence from MoS2 Monolayers by Mie-Resonant Metasurfaces. *ACS Photonics* **2019**, *6*, 1002−1009.

(10) Kruk, S.; Ferreira, F.; mac Suibhne, N.; Tsekrekos, C.; Kravchenko, I.; Ellis, A.; Neshev, D.; Turitsyn, S.; Kivshar, Y. Transparent Dielectric Metasurfaces for Spatial Mode Multiplexing. *Laser & Photonics Reviews* **2018**, *12*, 1800031.

(11) Tang, S.; Li, X.; Pan, W.; Zhou, J.; Jiang, T.; Ding, F. High-efficiency broadband vortex beam generator based on transmissive metasurface. *Opt. Express* **2019**, *27*, 4281−4291.

(12) Dong, Z.; Ho, J.; Yu, Y. F.; Fu, Y. H.; Paniagua-Domínguez, R.; Wang, S.; Kuznetsov, A. I.; Yang, J. K. W. Printing Beyond sRGB Color Gamut by Mimicking Silicon Nanostructures in Free-Space. *Nano Lett.* **2017**, *17*, 7620−7628.

(13) Zhu, X.; Yan, W.; Levy, U.; Mortensen, N. A.; Kristensen, A. Resonant laser printing of structural colors on high-index dielectric metasurfaces. *Science Advances* **2017**, *3*, e1602487.

(14) Ha, S. T.; Fu, Y. H.; Emani, N. K.; Pan, Z.; Bakker, R. M.; Paniagua-Domínguez, R.; Kuznetsov, A. I. Directional lasing in resonant semiconductor nanoantenna arrays. *Nat. Nanotechnol.* **2018**, *13*, 1042−1047.

(15) Polushkin, A. S.; Tiguntseva, E. Y.; Pushkarev, A. P.; Makarov, S. V. Single-particle perovskite lasers: from material properties to cavity design. *Nanophotonics* **2020**, *9*, 599−610.

(16) Yesilkoy, F.; Arvelo, E. R.; Jahani, Y.; Liu, M.; Tittl, A.; Cevher, V.; Kivshar, Y.; Altug, H. Ultrasensitive hyperspectral imaging and biodetection enabled by dielectric metasurfaces. *Nat. Photonics* **2019**, *13*, 390−396.

(17) Leitis, A.; Tittl, A.; Liu, M.; Lee, B. H.; Gu, M. B.; Kivshar, Y. S.; Altug, H. Angle-multiplexed all-dielectric metasurfaces for broadband molecular fingerprint retrieval. *Science Advances* **2019**, *5*, eaaw2871.

(18) Tittl, A.; Leitis, A.; Liu, M.; Yesilkoy, F.; Choi, D.-Y.; Neshev, D. N.; Kivshar, Y. S.; Altug, H. Imaging-based molecular barcoding with pixelated dielectric metasurfaces. *Science* **2018**, *360*, 1105−1109.

(19) Wang, H.; Ke, Y.; Xu, N.; Zhan, R.; Zheng, Z.; Wen, J.; Yan, J.; Liu, P.; Chen, J.; She, J.; Zhang, Y.; Liu, F.; Chen, H.; Deng, S. Resonance Coupling in Silicon Nanosphere−J-Aggregate Heterostructures. *Nano Lett.* **2016**, *16*, 6886−6895.

(20) Ruan, Q.; Li, N.; Yin, H.; Cui, X.; Wang, J.; Lin, H.-Q. Coupling between the Mie Resonances of Cu2O Nanospheres and the Excitons of Dye Aggregates. *ACS Photonics* **2018**, *5*, 3838−3848.

(21) Tserkezis, C.; Gonçalves, P. A. D.; Wolff, C.; Todisco, F.; Busch, K.; Mortensen, N. A. Mie excitons: Understanding strong coupling in dielectric nanoparticles. *Phys. Rev. B: Condens. Matter Mater. Phys.* **2018**, *98*, 155439.

(22) Todisco, F.; Malureanu, R.; Wolff, C.; Gonçalves, P. A. D.; Roberts, A. S.; Mortensen, N. A.; Tserkezis, C. Magnetic and Electric Mie-Exciton Polaritons in Silicon Nanodisks. *arXiv.org (Physics)*, submitted June 24, **2019**. https://arxiv.org/pdf/1906.09898.pdf.

(23) Wang, K.; Titchener, J. G.; Kruk, S. S.; Xu, L.; Chung, H.-P.; Parry, M.; Kravchenko, I. I.; Chen, Y.-H.; Solntsev, A. S.; Kivshar, Y. S.; Neshev, D. N.; Sukhorukov, A. A. Quantum metasurface for multiphoton interference and state reconstruction. *Science* **2018**, *361*, 1104−1108.

(24) Stav, T.; Faerman, A.; Maguid, E.; Oren, D.; Kleiner, V.; Hasman, E.; Segev, M. Quantum entanglement of the spin and orbital angular momentum of photons using metamaterials. *Science* **2018**, *361*, 1101−1104.

(25) Kruk, S.; Poddubny, A.; Smirnova, D.; Wang, L.; Slobozhanyuk, A.; Shorokhov, A.; Kravchenko, I.; Luther-Davies, B.; Kivshar, Y. Nonlinear light generation in topological nanostructures. *Nat. Nanotechnol.* **2019**, *14*, 126−130.

(26) Jackson, J. D. *Classical Electrodynamics*; John Wiley & Sons, Inc.: New York, 1999.

(27) Raab, R. E.; de Lange, O. L. *Multipole Theory in Electromagnetism: Classical, Quantum, and Symmetry Aspects, with Applications*; Oxford University Press on Demand: Oxford, 2005.

(28) Radescu, E. E.; Vaman, G. Exact calculation of the angular momentum loss, recoil force, and radiation intensity for an arbitrary source in terms of electric, magnetic, and toroid multipoles. *Phys. Rev. E: Stat. Phys., Plasmas, Fluids, Relat. Interdiscip. Top.* **2002**, *65*, 046609.

(29) Dubovik, V.; Tugushev, V. Toroid moments in electrodynamics and solid-state physics. *Phys. Rep.* **1990**, *187*, 145−202.

(30) Nemkov, N. A.; Basharin, A. A.; Fedotov, V. A. Electromagnetic sources beyond common multipoles. *Phys. Rev. A: At., Mol., Opt. Phys.* **2018**, *98*, 023858.

(31) Zografopoulos, D. C.; Algorri, J. F.; Ferraro, A.; García-Cámara, B.; Sánchez-Pena, J. M.; Beccherelli, R. Toroidal metasurface resonances in microwave waveguides. *Sci. Rep.* **2019**, *9*, 7544.

(32) Evlyukhin, A. B.; Fischer, T.; Reinhardt, C.; Chichkov, B. N. Optical theorem and multipole scattering of light by arbitrarily shaped nanoparticles. *Phys. Rev. B: Condens. Matter Mater. Phys.* **2016**, *94*, 205434.

(33) Gurvitz, E. A.; Ladutenko, K. S.; Dergachev, P. A.; Evlyukhin, A. B.; Miroshnichenko, A. E.; Shalin, A. S. The High-Order Toroidal Moments and Anapole States in All-Dielectric Photonics. *Laser Photonics Rev.* **2019**, *13*, 1800266.

(34) Grahn, P.; Shevchenko, A.; Kaivola, M. Electromagnetic multipole theory for optical nanomaterials. *New J. Phys.* **2012**, *14*, 093033.

(35) Alaee, R.; Rockstuhl, C.; Fernandez-Corbaton, I. An electromagnetic multipole expansion beyond the long-wavelength approximation. *Opt. Commun.* **2018**, *407*, 17−21.

https://dx.doi.org/10.1021/acsphotonics.0c00078
ACS Photonics 2020, 7, 1067−1075

(36) Alaee, R.; Rockstuhl, C.; Fernandez-Corbaton, I. Exact Multipolar Decompositions with Applications in Nanophotonics. *Adv. Opt. Mater.* **2019**, *7*, 1800783.
(37) Evlyukhin, A. B.; Chichkov, B. N. Multipole decompositions for directional light scattering. *Phys. Rev. B: Condens. Matter Mater. Phys.* **2019**, *100*, 125415.
(38) Rahimzadegan, A.; Arslan, D.; Dams, D.; Groner, A.; Garcia-Santiago, X.; Alaee, R.; Fernandez-Corbaton, I.; Pertsch, T.; Staude, I.; Rockstuhl, C. Beyond dipolar Huygens' metasurfaces for full-phase coverage and unity transmittance. *Nanophotonics* **2020**, *9*, 75−82.
(39) Mie, G. Beiträge zur Optik trüber Medien, speziell kolloidaler Metallösungen. *Ann. Phys.* **1908**, *330*, 377−445.
(40) Bohren, C. F.; Huffman, D. R. *Absorption and Scattering of Light by Small Particles*; John Wiley & Sons, Inc.: New York, 1998.
(41) Zenin, V. A.; Evlyukhin, A. B.; Novikov, S. M.; Yang, Y.; Malureanu, R.; Lavrinenko, A. V.; Chichkov, B. N.; Bozhevolnyi, S. I. Direct Amplitude-Phase Near-Field Observation of Higher-Order Anapole States. *Nano Lett.* **2017**, *17*, 7152−7159.
(42) Yang, Y.; Zenin, V. A.; Bozhevolnyi, S. I. Anapole-Assisted Strong Field Enhancement in Individual All-Dielectric Nanostructures. *ACS Photonics* **2018**, *5*, 1960−1966.
(43) Burrows, C. P.; Barnes, W. L. Large spectral extinction due to overlap of dipolar and quadrupolar plasmonic modes of metallic nanoparticles in arrays. *Opt. Express* **2010**, *18*, 3187−3198.
(44) Born, M.; Wolf, E. *Principles of Optics: Electromagnetic Theory of Propagation, Interference and Diffraction of Light*, 7th ed.; Cambridge University Press: Cambridge, 1999.

https://dx.doi.org/10.1021/acsphotonics.0c00078
ACS Photonics 2020, 7, 1067−1075